The Astrophysical Journal, 927:115 (10pp), 2022 March 1 https://doi.org/10.3847/1538-4357/ac4f5f
© 2022. The Author(s). Published by the American Astronomical Society.
OPEN ACCESS

Stellar Models of Betelgeuse Constrained Using Observed Surface Conditions

Tianyin Luo[1], Hideyuki Umeda[1], Takashi Yoshida[2], and Koh Takahashi[3]
[1] Department of Astronomy, Graduate School of Science, The University of Tokyo, 7-3-1 Hongo, Bunkyo City, Tokyo 113-0033, Japan; tianyin@ualberta.ca
[2] Yukawa Institute for Theoretical Physics, Kyoto University, Kitashirakawa Oiwakecho, Sakyo-ku, Kyoto 606-8502, Japan
[3] Max Planck Institute for Gravitational Physics, D-14476 Potsdam, Germany
Received 2021 June 17; revised 2022 January 14; accepted 2022 January 24; published 2022 March 9

Abstract

We study stellar models for Betelgeuse using the HR diagram and surface abundances as observational constraints. Previous studies on Betelgeuse have not systematically investigated the surface abundances, but we believe they can be impacted by, and thus be used as an observational constraint for various parameters such as initial mass, rotation, and overshoot scheme. We investigate stellar models with varying initial mass as they evolve past the main sequence, and we examine the red supergiant (RSG) properties in detail. For each mass, we vary the initial rotation up to $\sim$300 km s^{-1}, and test two different overshoot parameters. Overall, the acceptable initial mass range is 12–25 $M_\odot$, but for nonrotating models only, the range is decreased to 15–24 $M_\odot$. Also for rotating models, we find that $v/v_{\rm K} = 0.3$ is the upper limit for initial rotation, as more rapidly rotating models are unable to fit to Betelgeuse's surface abundances as an RSG. In addition, we report two possibilities for the current stage of evolution, core helium burning or core carbon burning and beyond. We find that certain 17 $M_\odot$ models could fit both stages. Finally, we discuss the implications of our results in the context of merger scenarios which have been suggested as a mechanism to attain the observed surface velocity of Betelgeuse.

Unified Astronomy Thesaurus concepts: Red supergiant stars (1375); Stellar rotation (1629); Stellar evolution (1599)

1. Introduction

Betelgeuse (also known as α Orionis) is one of the brightest M-type supergiants in the night sky. Due to its brightness and relative proximity, it has long been a popular target of observations, and especially being used as an archetype to study the properties of red supergiants (RSGs). Multiband observations of Betelgeuse have been plenty (Wilson et al. 1992; Burns et al. 1997; Uitenbroek et al. 1998), and its periodic variable behavior has also been well documented in the past decades (Goldberg 1984; Smith et al. 2009).

In late 2019, the star underwent a well-publicized dimming episode over several months (Guinan et al. 2019; Guinan & Wasatonic 2020), followed by an equally puzzling rapid rise in luminosity in 2020 (Sigismondi 2020). This dimming brought its brightness to levels below what is typically expected from its inherent variability (Harper et al. 2020b; Levesque & Massey 2020), generating speculation among both academics and the general public alike. There have been various suggestions to explain the dimming, such as conjectures which suggest an imminent supernova event, and other less exciting proposals where a shroud of dust that entered into our line of sight (Gupta & Sahijpal 2020; Harper et al. 2020a) or changes occurred in the star's photosphere (Dharmawardena et al. 2020).

Unfortunately, due to the difficulty in obtaining precise distance measurements (Harper et al. 2008, 2017), many of Betelgeuse's fundamental stellar properties remain uncertain. As a result, there is currently no clear consensus on Betelgeuse's evolution history, and thus we cannot immediately explain the dimming episode or predict its future course of evolution with only observations. With that taken into consideration, scientists have begun taking a different approach in the past several years with the aid of powerful computers. By calculating stellar models and then comparing their properties with Betelgeuse's observable properties, we can constrain the numerous variable parameters that impact stellar evolution (Meynet et al. 2013; Dolan et al. 2016; Wheeler et al. 2017; Nance et al. 2018; Joyce et al. 2020). The eventual goal is to construct a complete stellar model that conforms to Betelgeuse, and this will not only allow us to understand Betelgeuse's past and future, but also elucidate the detailed inner mechanisms of RSGs as a whole.

In particular, Dolan et al. (2016) calculated a grid of nonrotating models and found results which favored a progenitor mass of $20^{+5}_{-3} M_\odot$ that is ascending the red giant branch. Their choice of observable constraints included the luminosity, surface temperature, mass-loss rate, and radius. Surface abundances were also discussed, but were only used for their best-fit 20 $M_\odot$ model, for which they found an adequate match with observed values. Also, they had suggested that initial rotation could potentially allow less massive stars to satisfy Betelgeuse's constraints, but that was not something they investigated in their study. Another study by Wheeler et al. (2017), which was the first of a series of three papers called the Betelgeuse Project (Wheeler et al. 2017; Nance et al. 2018; Sullivan et al. 2020), examined both nonrotating and rotating models in the 15–25 $M_\odot$ range. However, their main purpose was to study the surface rotation of Betelgeuse, so they did not apply any observable constraints except the surface rotation and the HR diagram (albeit with rather large error bars). They found that regardless of initial mass, their models only produced fits for the surface rotation near the base of the red giant branch, and that rotation cannot be maintained at a satisfactory level as the star continues to evolve past that point.

Original content from this work may be used under the terms of the Creative Commons Attribution 4.0 licence. Any further distribution of this work must maintain attribution to the author(s) and the title of the work, journal citation and DOI.

Another recent study by Joyce et al. (2020) took a different approach. They used asteroseismic simulations in addition to hydrodynamical calculations, and their observational parameter of choice was Betelgeuse's pulsation periods, which included a ≈400 day cycle identified as the fundamental frequency, and a ≈185 day cycle which was described as the first overtone. Through the examination of their models' pulsation patterns, they were able to determine a best-fit initial mass value of 18–21 $M_\odot$, which is slightly stricter than that of Dolan et al. (2016). In addition, they were able to derive new radius and distance estimates, which were in good agreement with the values measured by Hipparcos.

Clearly, there are still some conflicting results regarding Betelgeuse's progenitor model and past evolution history, and this study is motivated by the prospect of filling in the gap in information left by the aforementioned studies. In this study, we investigate stellar models of a range of initial masses, including both nonrotating and rotating models, with a focus on the use of surface carbon, nitrogen, and oxygen (CNO) abundances as the observational constraints as the star evolves as an RSG. Up until now, the surface abundances have largely been neglected as a constraint parameter, as studies have not done an in depth investigation over a large number of models. The aim is to find the times during which a model can be a fit for Betelgeuse in order to identify viable progenitor model properties. And with the use of surface abundances, stellar parameters involved in the mixing process, such as the rotational velocity and overshoot parameter, can be focused on in particular. In the process, the mystery of Betelgeuse's current stage of evolution, which includes a discussion relating to the recent dimming episode that spurred speculation about a possible supernova, will also hopefully be better understood.

This paper is organized as follows. In Section 2, the theoretical model and parameters and the choice of the observational constraints are explained. In Section 3, the results of our calculations are presented. In Section 4, the results of this study are discussed in the context of contemporary literature. Finally in Section 5, an overall summary is provided.

2. Methods

2.1. Observational Constraints

For ease of comparison, observational constraints for the HR diagram used in this paper will be the same as those adopted by Dolan et al. (2016), namely $\log L/L_\odot = 5.1 \pm 0.22$ and $T_{\rm eff} = 3500 \pm 200$ K, where L and $T_{\rm eff}$ are the luminosity and effective temperature. The adopted surface temperature is the result of an average of the past studies as the surface temperature of Betelgeuse is known to vary, and the luminosity is derived from the distance measurement given by Harper et al. (2008). A new distance measurement was reported by Harper et al. (2017), but since it only differs from the 2008 results by 0.7σ, we stick with the 2008 results for ease of comparison. These same observational constraints are also used by Wheeler et al. (2017), although with three times the uncertainty.

Regarding the surface abundances, we adopt the observed abundances of CNO elements relative to hydrogen given in Lambert et al. (1984) as the constraint. However, when considering the observed values, it is important to consider its dependence on the surface temperature because Lambert et al. (1984) reported varying relative abundances in the range of 3600–3800 K. Dolan et al. (2016) argued that such a correlation in surface abundance and temperature could be neglected due to the inherent variability of Betelgeuse, and used the relative abundances at 3800 K as their constraint. However, we believe it is more suitable to use the values given for 3600 K, because the difference between the observed abundances at 3600 K and 3800 K is a non-negligible amount. Lambert et al. (1984) report an error of ±0.15 (units are in dex) for each element at 3800 ± 100 K, but we take the error range for our adopted surface abundance to be the difference between the values reported for 3600 K and 3800 K (see Figure 6 in their paper). This difference was 0.12 for carbon, and 0.25 for nitrogen and oxygen, but for the case of carbon, we have decided it is more sensible to use the larger 0.15 value. Thus, our constraints for the relative abundances are $\epsilon_{\rm C} = 8.29 \pm 0.15$, $\epsilon_{\rm N} = 8.37 \pm 0.25$, and $\epsilon_{\rm O} = 8.52 \pm 0.25$, where $\epsilon_i = \log(X_i/X_{\rm H}A_i) + 12$, X_i is the mass fraction of element i, $X_{\rm H}$ is the hydrogen mass fraction, and A_i is the average mass number of element i.

In addition, we also look at the ratio of N/O as another constraint, as it is a rather robust constraint that barely varies with respect to the surface temperature. From our adopted values, we find the logarithmic value of the N/O ratio is −0.15 (i.e., the difference between $\epsilon_{\rm N} - \epsilon_{\rm O}$), and the error range is ∼0.05 as reported in Lambert et al. (1984).

2.2. Model Description

For this study, we use the 1D stellar evolution code HOngo Stellar Hydrodynamics Investigator (HOSHI), which has been in continuous development by Takahashi et al. (2013, 2014), Takahashi (2018), and Yoshida et al. (2019). Stellar models are evolved from the zero-age main sequence (ZAMS) and are terminated when the central temperature reaches $\log T_c = 9.2$, approximately corresponding to the period between core carbon and neon burning. We follow the nuclear burning using the nuclear reaction network of 300 species of nuclei (Takahashi et al. 2018). Nuclear reaction rates are taken from the JINA reaclib database v1 (Cyburt et al. 2010), except for the ^{12}C(α, γ)^{16}O rate which is taken to be 1.2 times the value given in Caughlan & Fowler (1988). Evolution beyond this point is typically less than a few years and we assume that the red giant branch properties would not be strongly affected. We initially investigate 15, 17, 20, and 25 $M_\odot$ models, but we also add other models from 12 to 26 $M_\odot$ as necessary in order to determine the upper and lower limits for the initial mass. We consider the initial rotation and overshoot parameters as variables which can strongly affect the stellar evolution and the structure of that star.

2.2.1. Initial Rotation

The initial rotation is a parameter that is expected to have a large impact on the surface CNO abundances, as it applies a centrifugal effect as well as a meridian circulation effect to the star. In particular, the meridian circulation is a convective process where material is brought toward the surface along the axis of rotation, and flow toward the core occurs along the equatorial plane, and it plays a big role in the transportation of chemical elements to the surface (Huang 2004). In addition, rotation is known to favor convective mixing processes instead of inhibiting them (Maeder et al. 2008), so we also expect a larger initial rotation to result in more drastic changes in the

Table 1
Initial Surface Velocity

Mass ($M_\odot$)	v/v_K	v (km s^{-1})
15	0.1	79.0
	0.2	157.6
	0.4	296.1
17	0.1	81.0
	0.2	161.2
	0.4	315.1
20	0.1	83.9
	0.2	166.7
	0.4	328.9

model's surface abundances. When compared to nonrotating models, the rotation would also result in an increase of the core size, thus enhancing the production of CNO elements in the core regions, which would then be brought to the surface as the star evolves, through both the aforementioned convective process as well as during the dredge-up phase. These factors all combine to impact the surface abundances of the star as an RSG.

In HOSHI, angular momentum transport and the chemical mixing process induced by rotation are taken with a diffusive treatment. The included rotation effect is described in detail in Takahashi et al. (2014). The initial surface velocity is prescribed using the Kepler velocity, $v_K \equiv \sqrt{GM/R}$, where G is the gravitational constant and R is the stellar radius. The code then applies this velocity in the form of rigid body rotation for the ZAMS models. This should be considered a reasonable and sufficient assumption as the post-ZAMS evolution does not strongly depend on the star's formation history pre-ZAMS (Haemmerlé et al. 2013). For the initial rotation values, we have chosen $v/v_K = 0.1$, 0.2, and 0.4, and the exact velocity values when applied to the 15, 17, and 20 $M_\odot$ models can be seen in Table 1. These values were taken based off the report from Georgy et al. (2012) and Ekström et al. (2012), which found a critical velocity of approximately $v/v_{crit} = 0.4$ to be the average initial rotational velocity based on the observed main-sequence width on the HR diagram and the population of RSGs in our Galaxy. Here it should be noted that there is a slight discrepancy between v_{crit} and v_K, by a factor of $\sqrt{2/3}$. Indeed, when the values in Table 1 are compared with those of Ekström et al. (2012), we find that our velocities are approximately 9%–19% percent higher depending on the mass of the model. Nevertheless, these initial rotation values cover the range of values currently accepted to be characteristic of massive stars, and will be adequate for the purpose of this investigation.

2.2.2. Overshoot and Mixing

We also investigate the effects of varying the convective overshoot parameter. This parameter has implications on the mass of the helium core, which in turn will dictate the advanced stage evolution. In addition, convective flows are very efficient at mixing material, and are able to transport enriched material from the core up to the photosphere. For these reasons, we want to investigate its impact on the surface abundances of our stellar models as an RSG, in the context of Betelgeuse's observed properties. In particular, this parameter governs the physics at the core–envelope boundary, and describes a diffusive process where material in the convective core overshoots the boundary and mixes into the envelope. In HOSHI, this process is described in equation form for the diffusion coefficient as $D = D_0 \exp\left(\frac{-2\Delta r}{f_{ov} H_P}\right)$, where D_0 is the diffusion constant at the boundary, Δr is the distance from the boundary, f_{ov} is the overshoot parameter which can be varied, and H_P is the pressure scale height.

In short, we test two values for the overshoot parameter f_{ov} for the main sequence, 0.03 and 0.01, but f_{ov} is held constant at 0.002 after the core helium burning (characterized by central temperature $\log T_C \geqslant 8.7$). We believe that this is enough to probe into the impact of the overshoot parameter, as the majority of the impact on the surface abundances should result from core activity during the longer lasting main-sequence evolution. In this study, the naming conventions in Yoshida et al. (2019) will be followed, and the two overshoot models will be referred to as L_A ($f_{ov} = 0.03$) and M_A ($f_{ov} = 0.01$). These names stem from the fact those values were calibrated against early B-type stars in the Large Magellanic Cloud (Brott et al. 2011) and AB stars in open clusters of the Milky Way (Maeder & Meynet 1989; Georgy et al. 2012), respectively.

2.3. Other Parameters and Variables

We have chosen to ignore several other variables found in previous studies for a variety of reasons. First, we choose not to use the radius as an observational constraint due to its dependence on the highly uncertain distance measurement, as well its redundancy with the luminosity. However, we do discuss the radii of our models in the context of contemporary literature in Section 4.

Furthermore, the mass-loss rate applied to our models on the red giant branch is from de Jager et al. (1988), and is not varied among our models. According to Dolan et al. (2016), who examined various mass-loss rate parameterizations, the de Jager et al. (1988) rate is larger than their adopted observational rate of $2 \pm 1 \times 10^{-6}$ $M_\odot$ yr^{-1}, but they also note that their adopted value can only be considered a lower limit, and realistic modeling of the mass loss is complicated. Also, a recent study by Mauron & Josselin (2011) found that the measured mass-loss rate of several galactic RSGs agree well with the de Jager et al. (1988) prescription. Thus, we believe it is sufficient to use the de Jager et al. (1988) mass-loss rate for the purpose of this study.

Finally, in regards to the metallicity of Betelgeuse and RSGs, previous studies report a wide range of values. Ramírez et al. (2000) results show an [Fe/H] range of 0.05 ± 0.14, while Lambert et al. (1984), on the basis of Luck (1977, 1979), suggest an enhanced [Fe/H] value of up to ~0.2 is possible. Here $[\mathrm{Fe/H}] = \epsilon_{Fe} - \epsilon_{Fe,\odot}$ represents that relative abundance to solar values, and can be regarded as an overall indicator of metal abundance. In this study, the main elements of our focus are carbon, nitrogen, and oxygen, so we can look at the [CNO/H] values as a benchmark. From Section 2.1, we can calculate the total [CNO/H] of our adopted values at 3600 K to be 8.88. Our code defaults to the solar metallicity given in Asplund et al. (2009), which also gives [CNO/H] = 8.88. Thus, we believe that the solar metallicity models are sufficient for the purpose of this study.

Table 2
Summary of the Fit to Betelgeuse for All Models That Were Tested

Rotation	12 $M_\odot$		13 $M_\odot$		15 $M_\odot$		17 $M_\odot$		20 $M_\odot$		24 $M_\odot$		25 $M_\odot$		26 $M_\odot$	
(v/v_K)	L_A	M_A	L_A	M_A	L_A	M_A	L_A	M_A	L_A	M_A	L_A	M_A	L_A	M_A	L_A	M_A
no-rot	×	×	×	×	×	∘	∘	∘	∘	∘	×	∘	×	×	–	–
0.1	×	×	×	×	∘	∘	∘	∘	∘	∘	–	–	×	×	×	×
0.2	∘	×	∘	×	∘	×	∘	∘	×	∘	–	–	×	∘	×	×
0.3	–	–	–	–	×	×	×	∘	×	×	–	–	×	×	–	–
0.4	–	–	–	–	×	×	×	×	×	×	–	–	×	×	–	–

Note. ∘ represents a model that had a good fit for Betelgeuse on the red giant branch, × represents a model that did not, and – represents models that were not calculated.

3. Results

We have evolved models ranging from 12 to 26 $M_\odot$, with varying initial rotation values. As an overview, Table 2 shows a summary of all the models that were calculated, and whether or not they provided a good fit to Betelgeuse during their evolution, and Table 3 shows the timing of the fit for models labeled with ∘. For simplicity, we devise a naming scheme to identify each model, in the form *mmrrO*, where *mm* is a two digit number for the initial mass, *rr* refers to the initial rotation (*no* is nonrotating, *01* is $v/v_K = 0.1$, and so forth), and finally *O*, representing the overshoot parameter, is either *M* or *L*. For example, *15noM* would refer to a 15 $M_\odot$, nonrotating model with M_A overshoot.

In the rest of this section, we will provide detailed results on particular models. First, we will show the typical evolution of 15 $M_\odot$, nonrotating models as a reference. Following that, we will present the results of varying the other initial parameters.

3.1. Nonrotating 15 $M_\odot$ Models

Figure 1 shows the complete evolution of both the *15noM* and *15noL* models. In the case of the *15noM* model, the fit occurs during the very end of the evolution when the model is finally able to reach the observed luminosity error range. This fit lasts until the end of the evolution, approximately $\sim 1 \times 10^4$ yr, and covers the late core helium burning and core carbon burning stages.

On the other hand, the *15noL* model is able to attain a high enough luminosity very early during its red giant branch evolution, before the star has even experienced its first dredge-up. The star then contracts and begins to dim, but it will slowly recover the luminosity after it begins core helium burning.

Figure 2 shows the changes of the surface abundances during the evolution. The change in surface oxygen is insignificant, so we omit that plot, and instead the surface N/O ratio is shown, which is a much stricter constraint on our results. We can see that in the case of the higher $f_{ov} = 0.03$ overshoot L_A model, almost all of the changes in surface abundances occur during the dredge-up, and the abundances remain unchanged during the subsequent red giant branch evolution. As a result, the surface N/O ratio remains outside the error range and this model is not a good fit for Betelgeuse. On the other hand, in the lower $f_{ov} = 0.01$ overshoot model, the surface CNO abundances are constantly changing during the red giant branch evolution. This allows the model to become a good fit for Betelgeuse during the later stages of its evolution, including core helium and core carbon burning stages.

Table 3
Summary of the Fit Timings for All Models Marked with ∘ in Table 2

Mass ($M_\odot$)	Overshoot	v/v_K	$t_{col,u}$ (yr)	$t_{col,l}$ (yr)	t_{total} (yr)
12	L_A	0.2	5.90E+03	0	5.90E+03
13	L_A	0.2	1.25E+04	0	1.25E+04
15	L_A	0.1	9.81E+05	8.98E+05	1.00E+05
			2.17E+04	0	2.17E+04
		0.2	9.99E+05	8.96E+05	1.03E+05
			2.18E+04	0	2.18E+04
	M_A	no	1.31E+04	0	1.31E+04
		0.1	1.13E+04	5.96E+03	5.36E+03
17	L_A	no †	8.42E+05	6.57E+05	1.84E+05
			1.04E+05	0	1.04E+05
		0.1	8.38E+05	0	8.38E+05
		0.2†	8.38E+05	6.14E+05	2.24E+05
	M_A	no	2.15E+04	1.71E+04	4.41E+03
		0.1	2.69E+04	1.87E+04	9.21E+03
		0.2	9.29E+04	4.93E+04	4.36E+04
		0.3	8.60E+05	8.53E+05	6.88E+03
20	L_A	no †	8.66E+04	4.95E+04	3.71E+04
		0.1	7.30E+05	9.70E+03	7.20E+05
	M_A	no	3.47E+04	2.64E+04	8.21E+03
		0.1	7.52E+04	1.85E+04	5.67E+04
		0.2	1.76E+05	1.43E+05	3.29E+04
24	M_A	no	8.10E+04	7.19E+04	9.07E+03
25	M_A	0.2	2.92E+05	2.29E+05	6.27E+04

Note. t_{total} refers to the total time of the fit for that model. The time to collapse upper ($t_{col,u}$) and lower ($t_{col,l}$) limits refer to the time from the models' first and last time of good fit for Betelgeuse, respectively, until the end of the evolution. Models that had undergone a blue loop phase are marked with †. Some models have more than one period of good fit, which are listed on separate lines in chronological order.

3.2. Variation of Initial Rotation

In Figure 3, the HR diagrams of the $v_K = 0.1$ and 0.2 models are shown. The impact on the HR diagram by varying initial

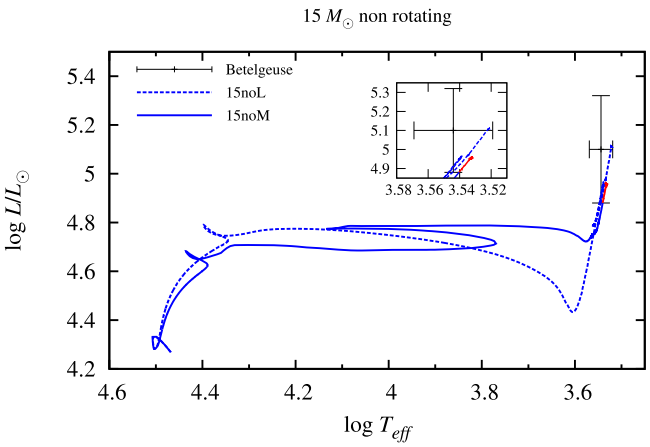

Figure 1. Evolution tracks for the nonrotating 15 $M_\odot$ models applied with different overshoot parameters. The inset plot is zoomed in and focused on the observed HR diagram position of Betelgeuse. The error bars are the same as those in Dolan et al. (2016). The period where the model satisfies Betelgeuse's observational constraints is indicated in red.

rotation is minuscule, and their evolution tracks are nearly identical.

Rather, the effect on the surface abundances is profound, and can be seen in Figure 4. The surface abundances are a limiting factor on the timing of the fit for Betelgeuse for these 15 $M_\odot$ models. For models of the same overshoot parameter, we can see the distinct monotonic relationship between the surface abundances of each CNO element and the initial rotation. For carbon and oxygen, higher initial rotation results in a lower abundance during the red giant branch evolution, while the reverse applies for surface nitrogen. An increase in the initial rotational velocity also leads to a change in surface abundance earlier during its evolution. This can be seen in models with $v/v_{\rm K} = 0.4$, where the onset of changes occurs almost at the beginning of the main-sequence evolution.

As a result, only a specific range of initial rotation values allow for the model to reproduce a fit for all observational constraints. As mentioned before, in the case of nonrotating 15 $M_\odot$ models, the *15noL* model was unsatisfactory due to the N/O ratio. However, referring back to Table 2, if the initial rotation is increased to $v/v_{\rm K} = 0.1$ or 0.2, then we find that the *1501M*, *1501L*, and *1502L* models are all able to produce a fit to Betelgeuse. Both L_A models fit until the end of the evolution, while the *1501M* model briefly fits for $\sim 5 \times 10^3$ yr near the very end of the evolution. Models with an initial rotation larger than $v/v_{\rm K} = 0.2$ also suffer from unsatisfactory N/O ratios, but in this case the surface nitrogen becomes much more abundant than the surface oxygen. This upper limit of the acceptable initial rotation at $v/v_{\rm K} = 0.2$ (or 0.3 for 17 $M_\odot$) is noteworthy, since our chosen initial rotation velocities were based on Georgy et al. (2012) and Ekström et al. (2012), who had suggested that $v/v_{\rm crit} = 0.4$ (or $v/v_{\rm K} \approx 0.33$) is a typical value to reproduce the RSG population in our Galaxy. This may suggest that the initial rotation velocity of Betelgeuse was slower than average or that the current prescription of the rotation induced mixing has a problem. In either case, efforts to reproduce rotating models would be considered worthwhile.

3.3. Variation of Initial Mass

The initial mass of a model mainly affects the luminosity during the evolution, but also can slightly affect the surface

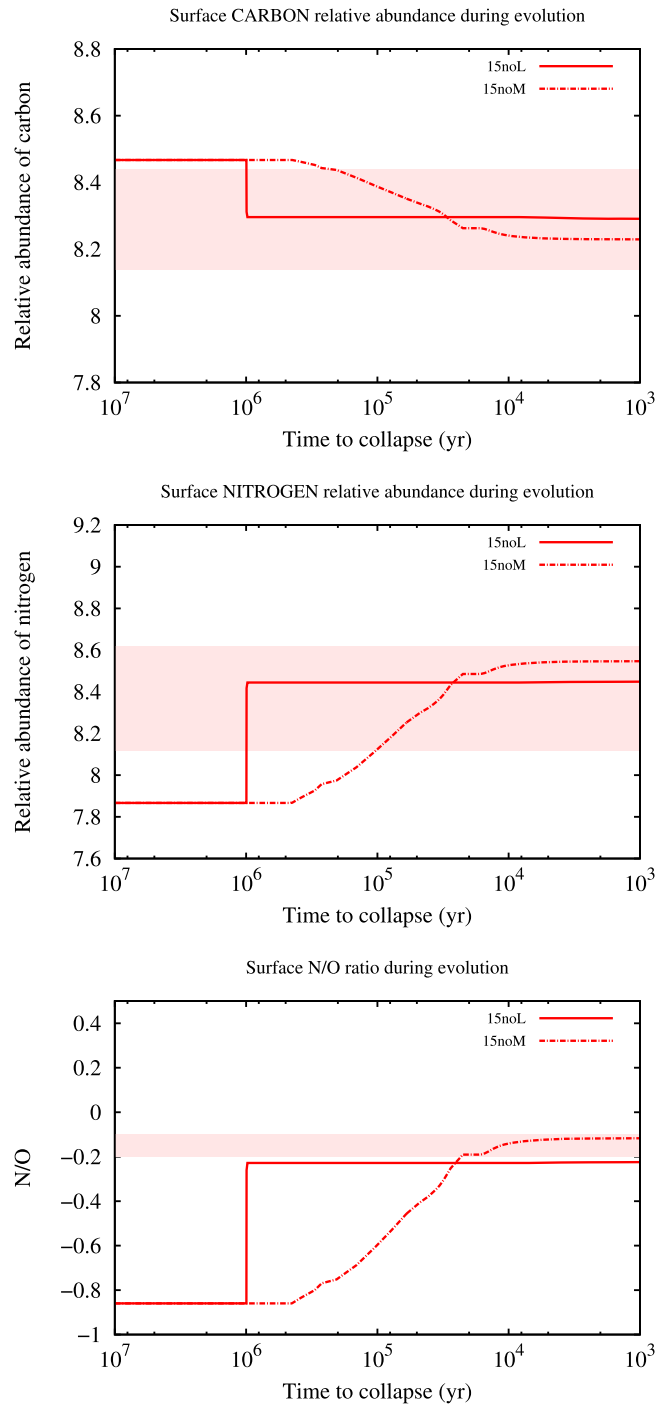

Figure 2. Relative surface abundances of carbon, nitrogen, and the surface N/O ratio for 15 $M_\odot$ models with no rotation. The top panel is carbon, the middle panel is nitrogen, and the bottom panel is the N/O ratio. Time to collapse refers to the time until the end of the evolution. The region shaded in red indicates the adopted observational constraints as given in Section 2. The solid lines are the L_A overshoot models, while the dashed lines are the M_A overshoot models.

abundances. From Figure 5, we can see that across models with the same initial rotation and overshoot parameter, the variation of the luminosity is large and becomes a limiting factor for many models at the extreme ends of the initial mass range. Overall, for the suitable initial mass range of the Betelgeuse progenitors, we find the lower initial mass limit at 12 $M_\odot$ with the model *1202L*. This model is extremely limited by its luminosity, only being able to fit for $\sim 6 \times 10^3$ yr at the very

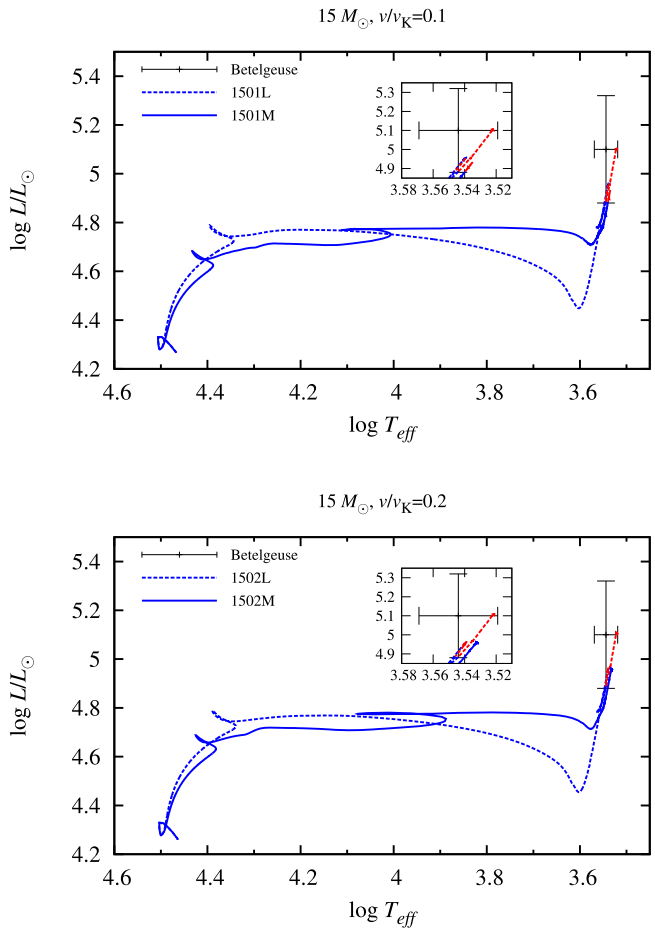

Figure 3. Evolution tracks for the 15 $M_\odot$ rotating models applied with different overshoot parameters. The inset plot is zoomed in and focused on the observed HR diagram position of Betelgeuse. The error bars are the same as those in Dolan et al. (2016). The period where the model satisfies Betelgeuse's observational constraints is indicated in red.

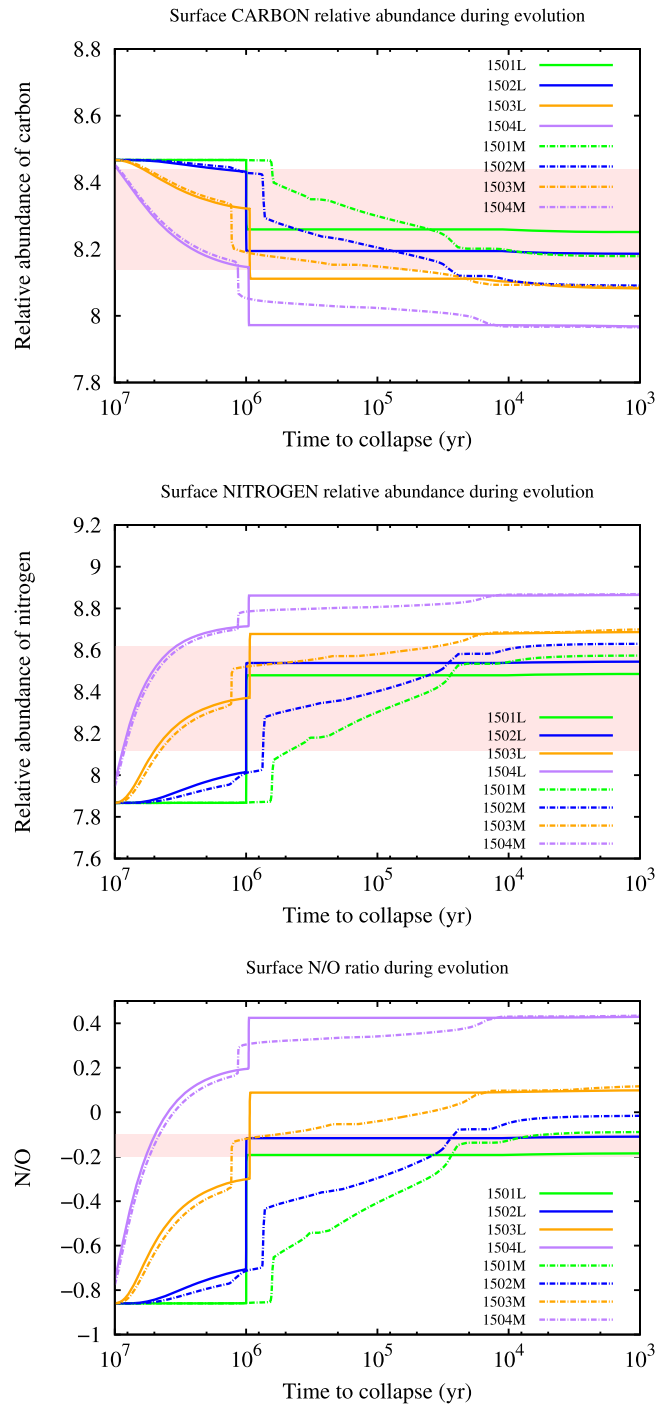

Figure 4. Same as Figure 2, but for the 15 $M_\odot$ models with varying initial rotation.

end of its evolution, indicating that any lower mass would not be viable. At the higher end of the initial mass range, we find a brief period of fit in the *2502M* model (not shown in Figure 5, but it is indeed limited by its luminosity). One noteworthy point is the overshoot parameter at both ends of the acceptable initial mass range, with the L_A overshoot required for the lower limit, and the M_A overshoot for the upper limit. Dolan et al. (2016) had suggested that that initial rotation would be key to allow lower mass models (i.e., $\leqslant 15\ M_\odot$) to fit to Betelgeuse, but our results suggest that an increase in the overshoot parameter is more crucial. In the 17–20 $M_\odot$ mass range, we see that our models maintain much longer periods of fit, as they spend their entire red giant branch evolution within the observed HR diagram constraints, and both overshoot parameters produce viable models. This does corroborate with the results from Dolan et al. (2016) and Joyce et al. (2020) that the best fit for the Betelgeuse's progenitor mass is in this range.

The impact of the initial mass on the surface abundances is much less dramatic, with the main differences arising in the N/O ratios. In Figure 6, we can see that all models regardless of initial mass show no change in surface abundances before the dredge-up, allowing all models to have a time period where they can fit to Betelgeuse's observed surface abundances. Also, larger masses have higher surface nitrogen and lower carbon and oxygen on the red giant branch, which allows the *17noL* model to fit to Betelgeuse until the end of its evolution, as opposed to the *15noL* model which has an insufficient N/O ratio of −0.23.

Considering that the mass of Betelgeuse is not readily measurable, it is generally the most important parameter to be derived from these numerical simulation studies. Dolan et al. (2016) favored a best-fit model with n initial mass of $20^{+5}_{-3}M_\odot$, currently ascending the red giant branch during core helium burning. They also suggested that initial rotation would be necessary for a lower mass model $\sim 15M_\odot$ to satisfy the luminosity of Betelgeuse. Joyce et al. (2020), using a different

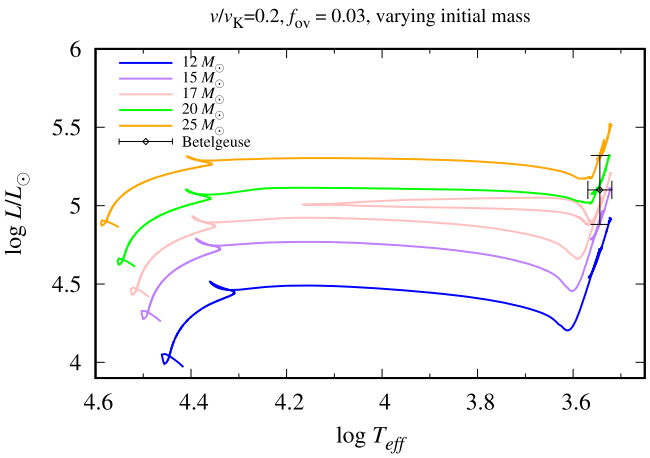

Figure 5. Evolution tracks for the 12–25 $M_\odot$ models with $v/v_K = 0.2$ and L_A.

approach of combined asteroseismic and hydrodynamical simulations, reported a model-derived initial mass of 18–21 $M_\odot$. In our study, with the use of surface abundances as observational constraints, we find viable models for both non- and initially rotating models between 12 and 25 $M_\odot$, depending on the initial parameters, such as the overshoot parameter.

4. Discussion

4.1. Current Stage of Evolution

Betelgeuse's current stage of evolution is still up for debate. The recent dimming episode has spurred some discussion around this topic, about the possibility that Betelgeuse could undergo an imminent supernova. Recent studies mostly label the supernova scenario as conjecture, mostly suggesting that the dimming is due to other mechanisms. Results from Dolan et al. (2016) and Wheeler et al. (2017) also limit Betelgeuse to the core helium burning phase. However, our results somewhat contradict this consensus, as shown in Figure 7, where we see several models that are able to fit Betelgeuse until the end of their evolution, suggesting the possibility that Betelgeuse could currently be in or even past the core carbon burning stage. In the lower panel of Figure 7, we can see that most M_A overshoot models can only fit for a period of time during core helium burning, and only the *15noM* model can fit until the end of the evolution. This outcome largely echoes the results from Dolan et al. (2016), who had only considered a lower overshoot parameter, but did not consider 15 $M_\odot$ models in their best-fit range. However, when we consider the possibility of the higher L_A overshoot models, we are able to find many models of differing initial masses and initial rotation, which can fit Betelgeuse until the end of its evolution.

The differences in our results also stem from the use of a different set of observational constraints that have not been systematically studied before. While this does mean that it is rather prone to error, as for example, the error range for surface nitrogen and oxygen abundances are quite large, the additional use of the N/O ratio allows us to put much tighter constraints on our results. Thus, we believe our results show that the possibility of an imminent supernova event cannot be entirely ruled out. Further studies to try and reproduce these results, such as using different stellar evolution code suites, or by obtaining more precise measurements of the surface abundances would be worthwhile.

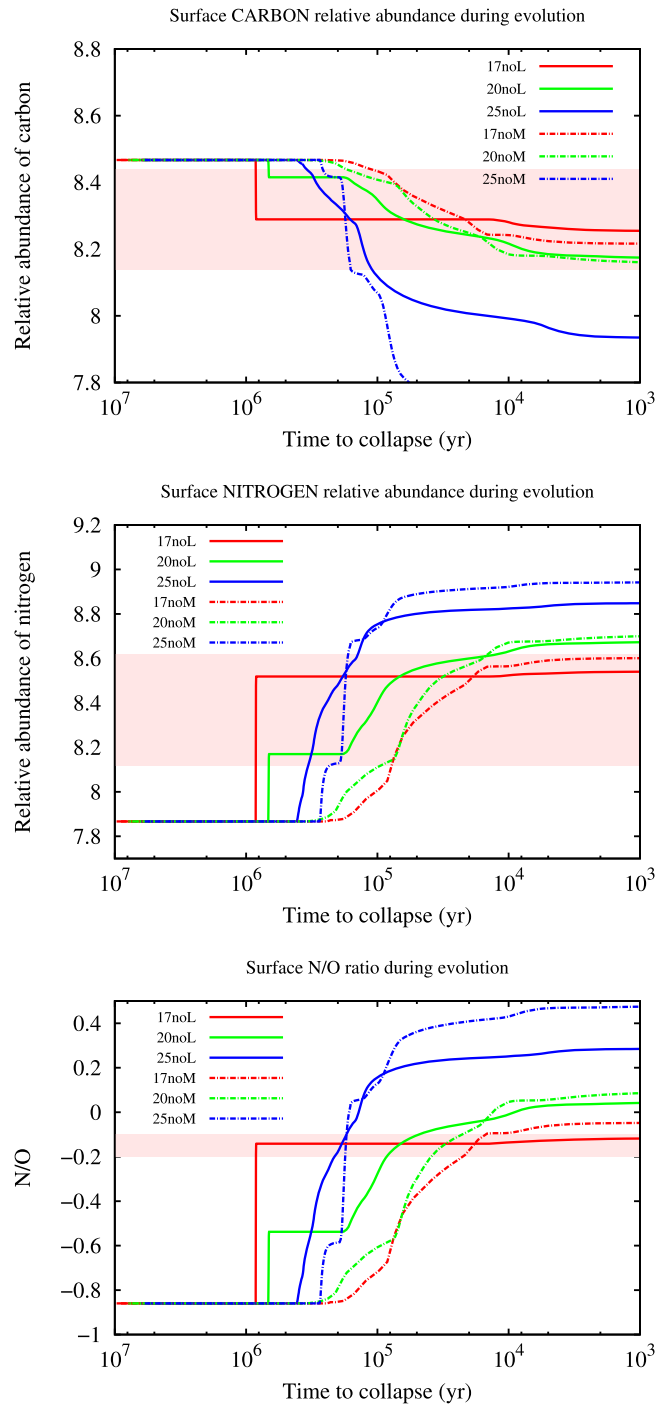

Figure 6. Same as Figure 2, but for the 17, 20, and 25 $M_\odot$ nonrotating models.

4.2. Blue Loop Phase

A small number of our models underwent a blue loop phase during helium burning, which affects our results for the total time of fit, for example the *1702L* model from Figure 5. These models are denoted by a † in Table 3. Blue loop phases are known to be related to a number of input parameters, for example Walmswell et al. (2015) discuss the implications of excess helium around the core and how it causes the blue loop. It has also been suggested that higher overshoot in the envelope would favor blue loop formation (Ritossa 1996), which would explain why we only find its existence in the L_A overshoot models. However, aside from the overshoot model, there is no

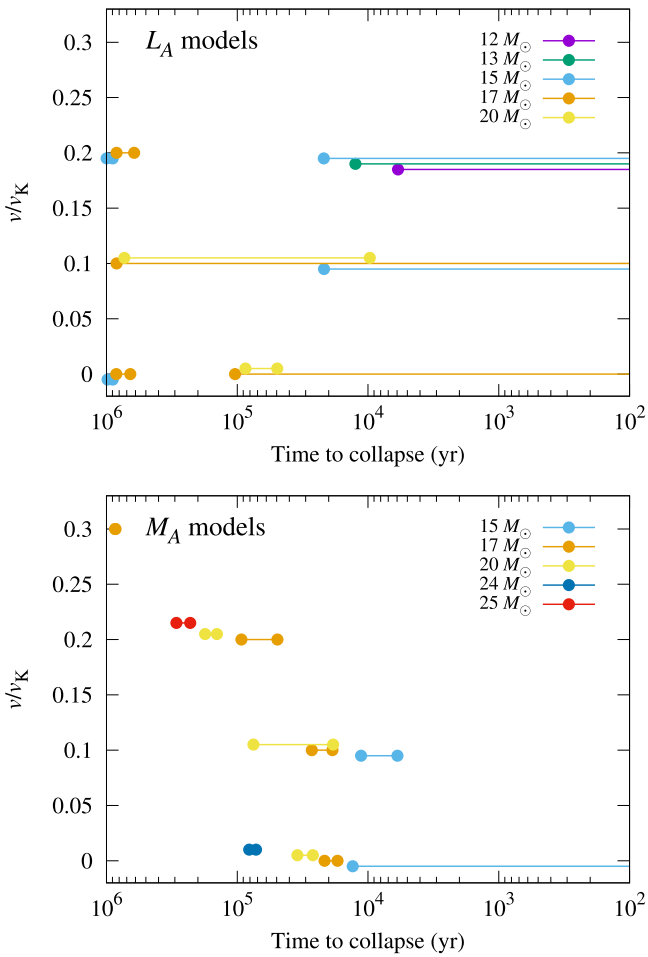

Figure 7. The timing of the fit for certain models with varying initial parameters, shown as a comparison.

discernible trend among our models as to what combination of initial conditions induces this loop phase. Both nonrotating and rotating models have blue loop models, and previous simulations using this code (see Yoshida et al. 2019, their Figure 12) also resulted in similar loop phases in their 18 $M_\odot$ models. Perhaps the occurrence stems from the calculation procedure, and is rather random in nature. Nevertheless, during the loop phase, the surface abundances remain largely unchanged, and only the change in the HR diagram position affects the fit for Betelgeuse. The loop phase occupies the majority of the helium burning phase, which results in shorter a total time of fit when compared to models without the loop phase. In our *17noL* and *1702L* models, the time spent in the loop outweighs the time spent within Betelgeuse's observed HR diagram error bars by roughly 5–3. However, due to the fact that stellar properties pre- and post-loop phase in our models are similar, we believe that the existence of the loop phase and its implications can be largely ignored in the context of its application to the Betelgeuse progenitor models.

4.3. Metallicity

In this study, we have focused on solar metallicity models, based on the surface abundances inferred from a surface temperature of 3600 K. However, it has been shown that the surface temperature of Betelgeuse is variable. If we instead consider the surface abundances for a higher surface temperature, such as 3800 K, then we would find the constraints from Lambert et al. (1984) to be $\epsilon_c = 8.41 \pm 0.15$, $\epsilon_N = 8.62 \pm 0.15$, and $\epsilon_O = 8.77 \pm 0.15$. Under these constraints, the corresponding [CNO/H] value is 9.10, meaning that the solar metallicity values we used would become unsuitable. Instead, we must adjust the metal content from [Fe/H] $\sim +0.1$ to $+0.2$ in order to find viable models. For reference, on the basis of the Asplund et al. (2009) solar abundances, if we increase the [Fe/H] to $+0.1$ or $+0.2$, the total [CNO/H] values become 9.06 and 9.17, respectively, and if we consider a middle ground of [Fe/H] $= +0.15$, the corresponding [CNO/H] value becomes 9.12.

Table 4
Summary of the Fit to Betelgeuse for the [Fe/H] = +0.15 Models

Rotation	15 $M_\odot$		17 $M_\odot$		20 $M_\odot$	
(v/v_K)	L_A	M_A	L_A	M_A	L_A	M_A
no-rot	×	×	∘	∘	∘	∘
0.1	×	∘	∘	∘	∘	∘
0.2	∘	×	∘	∘	×	∘
0.4	×	×	×	×	×	×

Note. In this case, the surface abundance constraints are $\epsilon_c = 8.41 \pm 0.15$, $\epsilon_N = 8.62 \pm 0.15$, and $\epsilon_O = 8.77 \pm 0.15$, as well as $N/O = -0.15 \pm 0.05$. ∘ represents a model with a good fit for Betelgeuse on the red giant branch, × represents a model that does not fit Betelgeuse during its evolution.

In Table 4, we have provided a simple overview of the viability of [Fe/H] $= +0.15$ using 15, 17, and 20 $M_\odot$ models, using the same observational constraints for everything aside from the surface abundances. We can see that despite the change in metallicity, the results are qualitatively similar to those for solar metallicity, except for the *1501L* and *15noM* models that are no longer viable.

However, the enhanced metallicity also causes the red giant branch to become cooler. Therefore, if we also impose different surface temperature constraints, certain models would have the timing of their fit impacted, or have their viability removed altogether. A previous study by Song et al. (2020) suggests that this reduction in surface temperature can be offset by increasing the mixing length parameter α, which has been kept at the default value of 1.8 in this study. We found that an increase of α to $\sim$2.0 is required to produce the results in Table 4 for a surface temperature increase of 200 K. Note although the mixing length parameter has been calibrated to $\alpha = 1.8$, it is not necessarily a fixed constant during evolution, and also does not rule out the possibility that Betelgeuse could behave similar to a model with a higher mixing length as Sonoi et al. (2019) have shown variation in the calibration of the mixing length parameter. Overall, we cannot use our results to determine the metallicity of Betelgeuse's progenitor model due to the large uncertainty of the surface temperature. The use of the mixing length parameter to make up for the surface temperature differences also complicates the matter.

4.4. Surface Rotation of Betelgeuse

So far we have neglected an important observational parameter which is Betelgeuse's surface rotation. At up to $v \approx 15\,\mathrm{km\,s^{-1}}$ (Kervella et al. 2018), Betelgeuse exhibits abnormally rapid rotation for an RSG, which proved to be

troublesome as none of our models were able to sustain high enough surface rotation into the helium burning stage.

The surface rotation of our models sharply drops as the star expands as a supergiant, and regardless of its initial rotation, the observed surface rotation velocity cannot be satisfied. This result also agrees with the main conclusion from Wheeler et al. (2017). In addition, various methods of angular momentum transport from the core to the surface, such as the (absence of) Tayler–Spruit dynamo effect (Heger & Langer 2000; Heger et al. 2005) or increasing viscosity (Wheeler et al. 2017), have also been proven to be ineffective at reproducing high surface rotation in RSGs.

There are emerging theories that attempt to explain Betelgeuse's rapid rotation, all of which involve Betelgeuse in a binary system in the past. One example is a merger theory, suggesting that Betelgeuse had absorbed a smaller companion during its evolution, which spun up its rotation. Recent studies have shown that a merger between a $\sim$15 and 20 $M_\odot$ during the ascent up the red giant branch (Chatzopoulos et al. 2020) or during the core helium or core carbon burning stages (Sullivan et al. 2020) can allow the model to attain satisfactory surface rotation as an RSG.

In our results, we have several models in the 15–20 $M_\odot$ range that present a good fit for Betelgeuse during and after the times of the proposed merger event. This suggests that if surface conditions were not greatly disturbed by the merger, our models could provide a complete reproduction of Betelgeuse's observed properties. Chatzopoulos et al. (2020) suggest that the surface conditions could change, or we could for see signatures of change during or after the merger, for example if the material mixed into the core regions induces additional mixing and material is brought up to the surface. However, Sullivan et al. (2020) argue that the inner structure changes in their post-merger models would not necessarily be accompanied by changes on the surface. In addition, there are scenarios where the merger material is distributed mostly into the outer regions of the primary, which still results in a spin-up but much less impact on the mixing processes, so our results cannot be completely ruled out as invalid in those cases.

Another example involves Betelgeuse being spun up through the accretion of mass from a larger companion over a period of time, and then being ejected by a supernova. This scenario is briefly discussed in Chatzopoulos et al. (2020), who referred to it as a possibility but less likely than the merger scenario, and mentioned that mixing of the accreted material deeper into the star could again alter its evolution. However, this accretion scenario has not been studied in depth, so we cannot draw any concrete conclusions of its impact on our results. We believe it is best to think of it similar to the merger scenario, where the most important point of consideration is how far the added material penetrates into the Betelgeuse model, and whether that could lead to significant changes of surface properties.

5. Summary

We have tested models of varying initial mass, initial rotation, and overshoot parameters using Betelgeuse's HR diagram position and surface CNO abundances as observational constraints. In our results, we found models of an initial mass between 12 and 25 $M_\odot$ as good fits for Betelgeuse. Models $\geqslant$15 $M_\odot$ can use either the M_A ($f_{\rm ov} = 0.01$) or L_A ($f_{\rm ov} = 0.03$) overshoot parameter, while $<$15 $M_\odot$ models require the higher L_A overshoot parameter to reach satisfactory luminosity. With regard to initial rotation, we found that both nonrotating and rotating models are able to produce good fits, but at masses near the lower and upper limits, only rotating models are viable. Also, above an initial rotation of $v/v_{\rm K} \sim 0.3$, surface conditions for an RSG do not match the observed values.

In some of our models, we found that the model is able to stay as a fit for Betelgeuse into core carbon burning or beyond, which differs from previous studies which placed Betelgeuse near the beginning of the red giant branch in core helium burning. This suggests that Betelgeuse could be closer to the end of its life than previous studies believe, and could undergo a supernova event soon.

Finally, Betelgeuse's current surface rotation remains an unsolved problem. While we have found promising candidates within our grid of models that can conform to both merger theories from Chatzopoulos et al. (2020) and Sullivan et al. (2020), the exact details of the post-merger models are still unclear. Complications arise when considering the surface composition of the post-merger model if the added material is mixed deep into the core regions of the primary. Such dramatic changes to the surface conditions would affect our results, so a comprehensive study on post-merger model properties compared with the observed values would be a logical next step. However, there is also the possibility that added material is mostly added to the outer envelope regions, in which case our results could provide a complete reproduction of Betelgeuse's observed properties.

Overall, we consider our results as contrary to previous studies, opening up new possibilities and discussions for Betelgeuse's current and past evolution. In future studies, we hope to find tighter limits on the progenitor model using more precise observational constraints in surface abundance and temperature, as well as better implementation of the overshoot parameters. Investigating the merger scenarios and the post-merger behavior with respect to those constraints will also hopefully shed light on their viability as a method to produce rapidly rotating RSGs like Betelgeuse.

This study was supported in part by the grants in aid for the Scientific Research of Japan Society for the Promotion of Science (JSPS) KAKENHI grant No. (JP17K05380, JP20H05249, JP20H 00158, and JP21H01123).

ORCID iDs

Hideyuki Umeda https://orcid.org/0000-0001-8338-502X
Takashi Yoshida https://orcid.org/0000-0002-8967-7063
Koh Takahashi https://orcid.org/0000-0002-6705-6303

References

Asplund, M., Grevesse, N., Sauval, A. J., & Scott, P. 2009, ARA&A, 47, 481
Brott, I., de Mink, S. E., Cantiello, M., et al. 2011, A&A, 530, A115
Burns, D., Baldwin, J. E., Boysen, R. C., et al. 1997, MNRAS, 290, L11
Caughlan, G. R., & Fowler, W. A. 1988, ADNDT, 40, 283
Chatzopoulos, E., Frank, J., Marcello, D. C., & Clayton, G. C. 2020, ApJ, 896, 50
Cyburt, R. H., Amthor, A. M., Ferguson, R., et al. 2010, ApJS, 189, 240
de Jager, C., Nieuwenhuijzen, H., & van der Hucht, K. A. 1988, A&AS, 72, 259
Dharmawardena, T. E., Mairs, S., Scicluna, P., et al. 2020, ApJL, 897, L9
Dolan, M. M., Mathews, G. J., Lam, D. D., et al. 2016, ApJ, 819, 7
Ekström, S., Georgy, C., Eggenberger, P., et al. 2012, A&A, 537, A146
Georgy, C., Ekström, S., Meynet, G., et al. 2012, A&A, 542, A29
Goldberg, L. 1984, PASP, 96, 366
Guinan, E. F., & Wasatonic, R. J. 2020, ATel, 13439, 1

Guinan, E. F., Wasatonic, R. J., & Calderwood, T. J. 2019, ATel, 13341, 1
Gupta, A., & Sahijpal, S. 2020, MNRAS, 496, L122
Haemmerlé, L., Eggenberger, P., Meynet, G., Maeder, A., & Charbonnel, C. 2013, A&A, 557, A112
Harper, G. M., Brown, A., & Guinan, E. F. 2008, AJ, 135, 1430
Harper, G. M., Brown, A., Guinan, E. F., et al. 2017, AJ, 154, 11
Harper, G. M., DeWitt, C. N., Richter, M. J., et al. 2020a, ApJL, 893, L23
Harper, G. M., Guinan, E. F., Wasatonic, R., & Ryde, N. 2020b, ApJ, 905, 34
Heger, A., & Langer, N. 2000, ApJ, 544, 1016
Heger, A., Woosley, S. E., & Spruit, H. C. 2005, ApJ, 626, 350
Huang, R. Q. 2004, A&A, 425, 591
Joyce, M., Leung, S.-C., Molnár, L., et al. 2020, ApJ, 902, 63
Kervella, P., Decin, L., Richards, A. M. S., et al. 2018, A&A, 609, A67
Lambert, D. L., Brown, J. A., Hinkle, K. H., & Johnson, H. R. 1984, ApJ, 284, 223
Levesque, E. M., & Massey, P. 2020, ApJL, 891, L37
Luck, R. E. 1977, ApJ, 212, 743
Luck, R. E. 1979, ApJ, 232, 797
Maeder, A., Georgy, C., & Meynet, G. 2008, A&A, 479, L37
Maeder, A., & Meynet, G. 1989, A&A, 210, 155
Mauron, N., & Josselin, E. 2011, A&A, 526, A156
Meynet, G., Haemmerlé, L., Ekström, S., et al. 2013, in EAS Publications Series, ed. P. Kervella, T. Le Bertre, & G. Perrin, Vol. 60 (Les Ulis: EDP Sciences), 17
Nance, S., Sullivan, J. M., Diaz, M., & Wheeler, J. C. 2018, MNRAS, 479, 251
Ramírez, S. V., Stephens, A. W., Frogel, J. A., & DePoy, D. L. 2000, AJ, 120, 833
Ritossa, C. 1996, MNRAS, 281, 970
Sigismondi, C. 2020, ATel, 13601, 1
Smith, N., Hinkle, K. H., & Ryde, N. 2009, AJ, 137, 3558
Song, N., Alexeeva, S., Sitnova, T., et al. 2020, A&A, 635, A176
Sonoi, T., Ludwig, H. G., Dupret, M. A., et al. 2019, A&A, 621, A84
Sullivan, J. M., Nance, S., & Wheeler, J. C. 2020, ApJ, 905, 128
Takahashi, K. 2018, ApJ, 863, 153
Takahashi, K., Umeda, H., & Yoshida, T. 2014, ApJ, 794, 40
Takahashi, K., Yoshida, T., & Umeda, H. 2013, ApJ, 771, 28
Takahashi, K., Yoshida, T., & Umeda, H. 2018, ApJ, 857, 111
Uitenbroek, H., Dupree, A. K., & Gilliland, R. L. 1998, AJ, 116, 2501
Walmswell, J. J., Tout, C. A., & Eldridge, J. J. 2015, MNRAS, 447, 2951
Wheeler, J. C., Nance, S., Diaz, M., et al. 2017, MNRAS, 465, 2654
Wilson, R. W., Baldwin, J. E., Buscher, D. F., & Warner, P. J. 1992, MNRAS, 257, 369
Yoshida, T., Takiwaki, T., Kotake, K., et al. 2019, ApJ, 881, 16